RSC Advances

PAPER

View Article Online
View Journal | View Issue

Cite this: *RSC Adv.*, 2017, **7**, 12856

Cerium-doped mesoporous-assembled SiO_2/P25 nanocomposites with innovative visible-light sensitivity for the photocatalytic degradation of organic dyes

Yan Jiang,[a] Zheng Jin,[a] Chen Chen,[a] Wubiao Duan,*[a] Bo Liu,[a] Xidong Chen,[a] Feihua Yang[b] and Jianping Guo[b]

SiO_2/P25 (SP) composites doped with different contents of cerium were prepared by a hydrothermal process at a relatively low temperature in this experiment. The resulting Ce–SiO_2/P25 (CSP) composites were successfully characterized by X-ray diffraction (XRD), X-ray photoelectron spectroscopy (XPS), scanning electron microscopy (SEM), high resolution transmission electron microscopy (HRTEM), N_2-physisorption, UV-vis diffuse reflectance spectroscopy (DRS), and photoluminescence spectroscopy (PL). The photocatalytic activities of the as-obtained catalysts were evaluated for the degradation of organic dyes, including Methylene Blue (MB) and Reactive Red 4 (RR4), under visible-light irradiation. The best results were obtained for a cerium loading of 5 mM. The CSP-5 nanoparticle showed the 91.8% decomposition of MB and 90.2% decomposition of RR4 in the liquid phase at room temperature under visible-light irradiation in a photoreactor, and the corresponding hydrogen evolution rate was 2.315 mmol g^{-1}, which was more efficient than that of pristine P25. Remarkably enhanced activities towards the photodecomposition of several organic compounds were observed depending on the synergistic effect between silicon and cerium. The Ce–SiO_2/P25 structure leads to efficient light harvesting into the visible-light region by forming new energy levels inside the nanoparticles and then electron–hole recombination could be effectively inhibited. The BET surface area measurement was used to provide an insight into the enhanced photocatalytic activity of the CSP composites, which was also understood to be because of the relative enhancement of the adsorption of organic molecules on the photocatalyst surface. In addition, the effect of the initial pH values on the photocatalytic degradation of different dyes using CSP-5 was investigated. Finally, a good recyclability of CSP-5 was demonstrated compared to that of pristine P25. Herein, the photocatalytic mechanism has been concretely explained.

Received 5th January 2017
Accepted 10th February 2017

DOI: 10.1039/c7ra00191f

rsc.li/rsc-advances

1. Introduction

The incomplete removal of organic dyes and other emerging pollutants in conventional wastewater treatment plants has been identified as the main route by which anthropogenic pollutants reach aqueous environments.[1] Consequently, the presence of dyes has become ubiquitous in natural waters, even to the extent of entering drinking water facilities.[2] Since Fujishima reported the generation of oxygen and hydrogen using titania electrodes under the irradiation of light in 1972,[3] photocatalysis has been regarded as one of the most effective and economical ways to remove organic pollutants from wastewater. Titanium dioxide (TiO_2) is the most used semiconductor for the photocatalytic degradation of organic compounds due to its interesting characteristics such as low-cost, non-toxicity, high stability, and high photocatalytic activity.[4] TiO_2 is widely used in photocatalysis,[5,6] self-cleaning coatings,[7] dye-sensitized solar cells,[8] nanoparticles-coated facemasks,[9] antibacterial coatings on medical devices,[10] and in optoelectronic and energy storage devices.[11] Commercial photocatalytic TiO_2 is usually available in the form of powder (Evonik Degussa Aeroxide P25) and has excellent activity. Its activity is based on the absorption of a photon of appropriate energy (about 3.2 eV) and the creation of charge carriers (holes-h^+ and electrons-e^-) that can oxidize organic pollutants into CO_2 and H_2O.[12–14] Despite such excellent properties of TiO_2, there are certain problems associated with TiO_2 that hinder its commercialization, including agglomeration of the nanoparticles,[15] which could result in a decrease in surface area upon thermal treatment,[16] the recombination of photogenerated electron–hole pairs,[17] the lack of visible-light photoactivity due to its wide band

[a]*Department of Chemistry, School of Science, Beijing Jiaotong University, Beijing 100044, China. E-mail: wbduan@bjtu.edu.cn; Tel: +86-10-51688409*

[b]*State Key Laboratory of Solid Wastes Resource Utilization and Energy Saving Building Materials, Beijing Building Materials Academy of Sciences Research, Beijing 100041, China*

gap ($E_g = 3.2$ eV),[18] and difficulty in recovery of the photocatalysts from aqueous suspension.

To solve most of these problems, titania and other functional metal oxide nanoparticles can be doped with thermally stable, low-cost, and high surface area materials, such as SiO_2, ZrO_2, MoO_3, and Fe_2O_3.[8,19] Silica is one of the best materials for preparing cerium-doped SiO_2/TiO_2 materials due to its surface chemistry and adsorption capacity,[20] easy and controllable preparation by the Stöber method,[21] optical transparency in the TiO_2 absorption region, and high thermal and mechanical stability.[22] Its surface silicon hydroxyl groups are beneficial for the adsorption of pollutants and the incorporation of an amorphous phase is effective to minimize the agglomeration of TiO_2 particles.[23,24] For example, some literature studies have reported SiO_2–TiO_2 heterogeneous systems exhibiting better photocatalytic activity than pristine TiO_2 probably since the adsorption of organic compounds was improved and the aggregation of TiO_2 nanoparticles was minimized, thus leaving a higher exposed surface area. They also reported that the photocatalytic activity and thermal stability of SiO_2-coated TiO_2 nanoparticles can be enhanced more efficiently than pure TiO_2 powder.[25–30]

It is recognized that the impurities induced by metal ions doping into the TiO_2 could efficiently narrow its band gap and extend the absorption edge into the visible-light range, thus improving the photocatalytic activity of TiO_2 under visible-light irradiation.[31–34] Among these, TiO_2 doped with Ce ions has stimulated extensive research attention due to its special 4f electron orbital structure, which can increase the separation rate of photogenerated charges.[35–37] Cerium is the most favored dopant among the lanthanide ions due to its low cost and ability to shift between CeO_2 and Ce_2O_3 in oxidizing and reducing conditions.[38] Previous studies have confirmed that the variable valences of Ce, such as Ce^{4+} and Ce^{3+}, make TiO_2 possess excellent characteristics for transferring electrons and enhancing the visible-light-absorption capability.[39] In addition, cerium doping increases the formation of oxygen vacancies with a relatively high transfer capacity of oxygen species.[40] Electronically, the effect of cerium on the band gap of TiO_2 has been explained as being due to an n-type impurity band at the interface between the titanium and cerium oxides.[41]

In this study, first, visible-light-activated cerium-doped SiO_2/P25 (CSP) nanocomposites were synthesized by the common hydrothermal method which has been extensively employed. The synthesized cerium-doped SiO_2/TiO_2 materials were thoroughly characterized by XRD, N_2 adsorption–desorption, SEM-EDS, TEM, XPS, UV-vis diffuse reflectance spectroscopy, and PL to determine their morphology and structural and optical properties. Second, both Methylene Blue (MB) and Reactive Red 4 (RR4) were selected as target contaminants to evaluate the photocatalytic activity of the cerium-doped SiO_2/P25 under visible-light irradiation. Organic dyes frequently occur globally in water sources and can severely affect the health of humans and animals when consumed in toxic water or when exposed to them. In particular, either cationic MB or anionic RR4 is one of the most commonly found organic dyes in surface waters that serve as sources of drinking water supply. In this study, the application of the cerium-doped SiO_2/P25 for the treatment of water contaminated with MB and RR4 was evaluated.

2. Experimental

2.1. Materials

All the reagents and solvents used for the synthesis and analysis of the catalysts were commercially available and used as received without further purification. Commercially available TiO_2 in powder form P25 was from Evonik (Germany). Reactive Red 4 dye (RR4, chemical formula: $C_{32}H_{23}ClN_8Na_4O_{14}S_4$) and Methylene Blue (MB, chemical formula: $C_{16}H_{18}ClN_3S$) simulated as the organic pollutants were provided by Aladdin. Cerium nitrate hexahydrate ($Ce(NO_3)_3 \cdot 6H_2O$, 99.99%) and tetraorthosilicate (TEOS, 99.99%) were purchased from Sigma-Aldrich and used as the cerium and silicon source, respectively. Absolute ethanol and deionized water were used for the preparation of the catalysts. Furthermore, hydrochloric acid and sodium hydroxide solution were used to adjust the initial pH values of the organic dye solution in the photocatalytic experiments. Table 1 provides a summary of the organic pollutants models used in this work.

2.2. Methods

2.2.1. Preparation of the Ce–SiO_2/P25 (CSP) composites. The modified catalysts were prepared by the following steps. 2.0 g of P25 nanoparticle was first suspended in 50 mL of deionized water with sodium hexametaphosphate serving as the dispersant by ultrasonic dispersion for 30 min. The solution was under continuous stirring while 2.5 mL TEOS and an appropriate amount of $Ce(NO_3)_3$ solution was added dropwise at a slow speed. The pH of the solution was adjusted to 7. Then, the suspension was transferred to a Teflon-lined stainless steel autoclave, followed by a hydrothermal treatment at 130 °C for 12 h. Finally, the CSP composites were washed with deionized water and ethanol repeatedly and dried under vacuum at 80 °C for 12 h. For short, hereafter CSP-1, CSP-3, CSP-5, and CSP-7 denote the samples prepared in 1, 3, 5, and 7 mM $Ce(NO_3)_3$ solution, respectively. For comparison, SiO_2/P25 (SP) was prepared as well following the same route, with and without the addition of the corresponding dopant.

2.2.2 Characterization techniques. The crystal phase of the materials was characterized by X-ray diffraction (XRD) and patterned as a collection in a 2θ range from 10° to 80° using a RIGAKU Ru-200B diffractometer equipped with Cu Kα irradiation at a scan rate of 0.5° s^{-1}. The average crystallite size was determined from the broadening of the diffraction peak using the Scherrer formula ($d = K\lambda/\beta \cos\theta$). The particles morphology and size distribution were examined by high resolution transmission electron microscopy (HRTEM, Tecnai G2 F20) and field-emission scanning electron microscopy (FE-SEM, Hitachi-S4800). The BET surface area was determined by a multipoint method on a Micromeritics ASAP 2020 using the adsorption data in the relative pressure range (P/P_0) of 0.02–0.45. Prior to the analysis, the samples were degassed for 6 h at 150 °C under vacuum (10^{-5} mbar) in the degas port of the adsorption analyzer, and the specific surface area was calculated by the

Table 1 Summary of the organic pollutants in this study

Organic pollutants	Chemical structure	Chemical formula	Molar mass (g mol^{-1})	λ_{max} (nm)
Methylene Blue	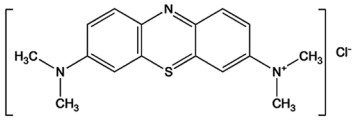	$C_{16}H_{18}ClN_3S$	319.85	664
Reactive Red 4	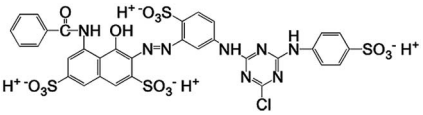	$C_{32}H_{23}ClN_8Na_4O_{14}S_4$	995.23	517

Brunauer–Emmett–Teller (BET) method. X-ray photoelectron spectroscopy (XPS) was obtained on a dual anode VG Microtech X-ray source and a Thermo Scientific ESCALAB 250Xi analyzer. A Cary 5000 UV-vis diffuse spectrophotometer was used to acquire the solid-state absorption and diffuse reflectance spectra (DRS) of the materials within the 200–800 nm range. The band gap values were evaluated using the Tauc Plot method by plotting $(\alpha h\nu)^{1/2}$ *versus* $h\nu$ (photon energy, eV), where α is the absorption coefficient, considering that all the solids are indirect semiconductors, like TiO_2.[42] The photoluminescence emission spectra (PL, FLS-980) were tested to investigate the recombination of photogenerated electron–hole pairs. The samples were excited at 280 nm.

2.2.3. Photocatalytic degradation. The photocatalytic activity of the different photocatalysts were evaluated by monitoring the degradation of cationic MB and anionic RR4 dye, respectively. The experiments were carried out at room temperature in a photoreactor (XPA-7) with a 500 W xenon lamp as the irradiation source, which was surrounded by all the cylindrical containers and placed 10 cm away from these containers. 100 mg of all the prepared catalysts were suspended in 100 mL aqueous solutions of the organic dyes with the concentration of 25 mg L^{-1} in a beaker. Prior to irradiation, the system was placed in a total dark environment under magnetic stirring for 45 min to investigate the adsorption behaviors of the photocatalysts. Following this, the photocatalytic reaction was started by exposure to visible light. During the reaction process, vigorous agitation was performed in each container to guarantee the uniform irradiation of the photocatalysts. A certain solution of organic dye was taken out at regular intervals of 15 min and analyzed after centrifugation followed by filtration to remove the catalyst particles. The degradation efficiency of the pollutants was measured by detecting the absorbance at their maximum absorption wavelength (λ_{max}) using the UV-vis spectrophotometer. The photometric analyses of all the photocatalysts could be carried out by measuring the degradation efficiency of dye (D%), which is defined by the following expression:

$$D\% = \frac{C_0 - C}{C_0} \times 100\% \quad (1)$$

where C_0 is the initial concentration of organic dye once the adsorption equilibrium was reached before lighting the lamp and C is the concentration of them after irradiation of the samples in the desired time interval. All the samples were tested under the same experimental conditions.

2.2.4. Stability tests of the photocatalysts. To evaluate the stability of the photocatalysts, a recycled usage experiment was carried out. Here, 100 mg of CSP-5 photocatalyst was suspended in 100 mL of a 25 mg L^{-1} solution of the dye and irradiated under a xenon lamp for 90 min. The sample was then centrifuged and the residues were collected, washed by distilled water and ethanol, then dried in the oven at 80 °C. Finally, this photocatalyst was reused again for the second cycle of degradation with a fresh dye solution. This process was repeated up to 5 times of application.

2.2.5. Photoelectrochemical experiments. To determine the photoelectrochemical characteristic of all the catalysts, experiments involving photocatalytic water splitting to generate hydrogen were carried out at ambient temperature and atmospheric pressure. Various photocatalyst powders were fabricated *via* the procedure reported by Ito *et al.*[43] to produce electrodes. The experiment was processed in a quartz photoreactor with a three-electrode configuration using the P25 and the prepared photocatalysts as the working electrode, a Pt wire as the counter electrode, and Ag/AgCl as the reference electrode, which were immersed in the electrolyte containing 100 mL of a 20 vol% ethanol and distilled water mixed solution. Prior to irradiation, the suspension of the catalysts was dispersed by an ultrasonic clean for 10 min and then the system was evacuated for 30 min to ensure the reactor was in an anaerobic condition. A xenon lamp located above the reactor was used as the light source. The generated gas was collected by a probe in 30 min intervals and analyzed using gas chromatography (GC-14C) with N_2 as the carrier flowing at 20 mL L^{-1}. The photocatalytic activities of the different samples were evaluated by the H_2 evolution rate in the same concentration range.

3. Results and discussion

3.1. XRD analysis

To investigate the crystal structure of the prepared catalysts, XRD measurements were performed. Fig. 1 shows the typical XRD patterns of the prepared samples. All the samples had similar patterns, which were dominated by a mixture of the anatase and rutile phases of TiO_2. The diffraction peaks of all the samples at 2θ values of 25.3°, 37.8°, 48.0°, 53.9°, 55.1°, 62.7°,

68.9°, 70.3°, and 75.1° could be perfectly indexed to the (101), (004), (200), (105), (211), (204), (116), (220), and (215) crystal planes of anatase TiO_2. Moreover, the patterns also clearly showed peaks of rutile TiO_2, namely, the planes (110), (101), and (111) at 2θ values of *ca.* 27.4°, 36.1°, and 41.2° respectively. There was also no phase transformation for all the as-obtained samples. According to Zhang *et al.*,[44] they observed the occurrence of phase transformation of TiO_2 only when the temperature was at 900 °C. The particle sizes were calculated from the Scherrer equation for all the samples from the most intense diffraction peak (101) corresponding to the peak at 2θ 25.31°, and coincident with the information specified from the producers. The equation used was as follows:

$$d = \frac{K\lambda}{\beta \cos \theta} \quad (2)$$

where d is the average thickness of the crystal in a direction normal to the diffracting plane (hkl), β is the crystallite size contribution to the peak width at half maximum intensity in radians, and K is the Scherrer constant. The crystallite sizes were 35.4, 31.3, 26.4, 22.6, 20.3, and 19.8 nm for P25, SP, CSP-1, CSP-3, CSP-5, and CSP-7, respectively. P25 showed good crystallinity at all major 2θ positions for the anatase phase. A strong reduction in the diffraction line intensity of anatase could be seen in the SP and CPS samples. This does not reflect the degradation/transformation of the anatase phase but is rather a result of the X-ray diffractions of an additional guest phase of amorphous silica, thus reducing the TiO_2 concentration in the mixture.[45] On the other hand, it should be noted that the ionic radius of Ce^{4+} (0.101 nm) is much bigger than that of Ti^{4+} (0.068 nm), and therefore it is difficult for Ce^{4+} to replace Ti^{4+} in the crystal lattice. Also, no crystalline phase related to cerium oxides could be found, confirming that it is unlikely for Ce^{4+} to enter the TiO_2 structure. In light of the ionic radii, as lanthanide ions are much larger than Ti^{4+}, these cerium ions tended to bond to oxygen anion on the surface of titania. Therefore, the decrease in the crystal size might be attributed to the presence of Ce–O–Ti bonds on the surface of the doped samples, which inhibit the growth of crystal grains.[46,47]

3.2. N_2 adsorption–desorption analysis

Gas physisorption is extensively used in the characterization of porous solids, particularly for evaluation of their specific surface area and total pore volume as well as their surface properties. The shape of the isotherm obtained from these adsorption measurements is very important as it can reveal the kind of porosity (micro-, meso-, or macroporosity) present in the sample. The differences in isotherms types and hysteresis loops can clearly be seen in Fig. 2. All the samples exhibit type IV sorption isotherms, while P25 shows an isotherm type II.[48] Also, it can be clearly observed that all the modified samples led to a marked change in the shape of the hysteresis loop in comparison to P25, showing a partial collapse of the ordered pore arrangement into a disordered pore arrangement, which finds some supporting evidence also in the SEM, TEM, and XRD analyses. These samples exhibited sorption isotherms with a relatively narrow hysteresis loop of an H_2 type, which is often attributed to porous inorganic oxides,[49] which indicates that the powders had a mesoporous structure with a narrow slit-like shape,[50] while P25 was reflected by the H3 hysteresis. The structural parameters determined on the basis of these isotherms are listed in Table 2. The results indicated that the P25 sample had the lowest surface area (84.67 $m^2\ g^{-1}$), but with the introduction of Si and Ce in the sample, an increase in the surface area was observed. Among all the photocatalysts, the surface area of CSP-5 was found to be the highest at 226.50 $m^2\ g^{-1}$. Also, the surface area of the CSP samples exceeded the sum of the SiO_2/P25 and pristine P25 samples, hence this enhanced the dispersity of the active component on the surface of the catalysts, which is beneficial for photocatalytic activity. At a higher dopant concentration, the well-dispersed CeO_2 species obstructed the pores and the active sites of TiO_2, which thus decreased the specific surface area.

3.3. XPS analysis

X-ray photoelectron spectroscopic analysis was employed as an important characteristic method to detect the chemical states of

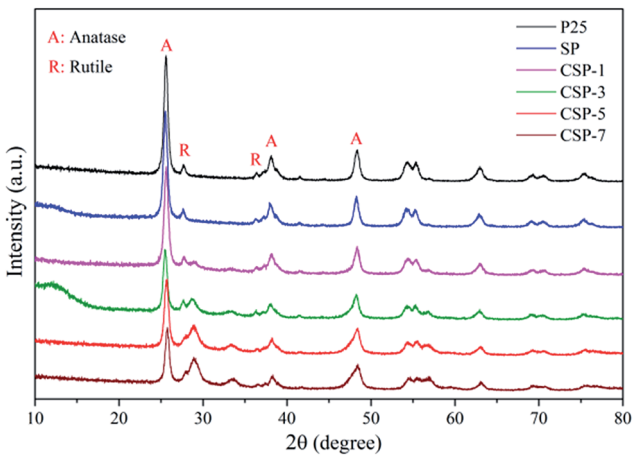

Fig. 1 XRD patterns of all the catalysts.

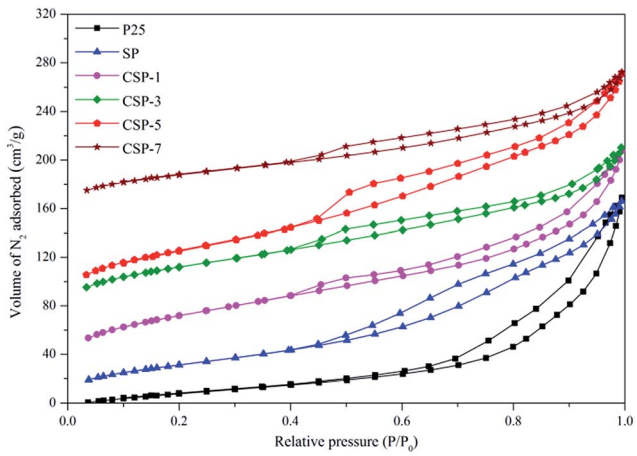

Fig. 2 N_2 adsorption–desorption isotherms of the P25, SP, and CSPs catalysts.

Table 2 Structural parameters of different catalysts

Samples	Crystal size (nm)	S_{BET} (m^2 g^{-1})	V_{tot} (nm)
P25	35.4	84.67	0.201
SP	31.3	147.59	0.241
CSP-1	26.4	162.81	0.314
CSP-3	22.6	205.38	0.363
CSP-5	20.3	226.50	0.412
CSP-7	19.8	219.55	0.387

the different species in the CSP samples. The XPS survey spectrum of the CSP-5 catalyst shown in Fig. 3a indicated that five elements of Ti, O, C, Si, and Ce existed on the surface of the CSP-5 sample. The carbon residue in the catalyst might be attributed to the carbon not being burned off completely during the heat treatment. The high resolution XPS spectrum with scanning over the area corresponding to the binding energies for the Ti 2p region is analyzed in Fig. 3b. The representative Ti 2p XPS spectrum indicates two peaks located at 458.9 eV and 464.5 eV, assigned to Ti $2p_{3/2}$ and Ti $2p_{1/2}$, which agree with the values of Ti^{4+} in a tetragonal structure.[51,52] The O 1s spectra of the CSP-5 sample is illustrated in Fig. 3c. The spectrum shows two types of peaks for the oxygen in the sample. The dominant peaks located at 529.8 eV agree with the O 1s electron binding energy of the lattice oxygen for TiO_2.[53] And the fitting data at 533.1 eV should be assigned to a Si–O bond. The Si 2p core region is shown in Fig. 3d, which verifies the formation of an interfacial Ti–O–Si bond between TiO_2 and SiO_2. The Si 2p line of CSP-5 can be best fitted as two doublets. The main peak at the binding energy (BE) of 103.7 eV corresponds to a Si–O–Si bond,[54] while the extra component that occurs at a 1.6 eV lower BE may be assigned to the Si–O–Ti bond. It turned out that a shift of electron density from the Ti to Si atom through an intermediate O atom led to a decrease in the BE of the Si atom, which confirmed the formation of an interfacial Si–O–Ti bond.[22] The XPS spectrum for Ce 3d is revealed in Fig. 3e. The Ce 3d spectra can be split into four pairs of spin-orbital bands ($3d_{5/2}$ and $3d_{3/2}$ denoted as v and u, respectively): v/u, v′/u′, v″/u″, and v‴/u‴, where the v/u, v″/u″, and v‴/u‴ peaks are associated with the characteristic chemical states of Ce^{4+}, while v′/u′ corresponds to that of Ce^{3+}.[55] The Ce species present in both forms of Ce^{3+} and Ce^{4+}, which shows that the surface of the catalyst was not fully oxidized, suggests the existence of oxygen vacancies. The Ce species are beneficial for the shift of the absorption toward the visible region and leads to a charge imbalance, thereby yielding oxygen vacancies and unsaturated chemical bonds. Thus, additional adsorbed oxygen species were generated on the surface of CSP-5, thus improving the photocatalytic degradation activity.[56]

3.4. Morphological and structural properties

The morphologies of P25 and CSP-5 were examined by FE-SEM and HRTEM, with the corresponding images shown in Fig. 4 and 5. The representative FE-SEM images show that the pure P25 had smooth spherical particles (Fig. 4a), while the surface of CSPs was rougher and decorated with small SiO_2 nanoparticles (Fig. 4b–e). The images of different concentrations of the Ce-doped samples are shown in Fig. 4b–e and indicate that the spherical aggregates of particles exhibited varying sizes, which was affected by the presence of silicon and cerium. In addition, Fig. 4 shows other FE-SEM images of P25 and CSP-5 together with the EDX spectrum of the Ti, O, Si, and Ce elements. From Fig. 4g, it can be seen that the elements of Ti, O, Si, and Ce were detected with random selection, confirming the presence of Si and Ce on the TiO_2 nanoparticles. The EDX analysis results give the atomic percentages of Ti, O, Si, and Ce

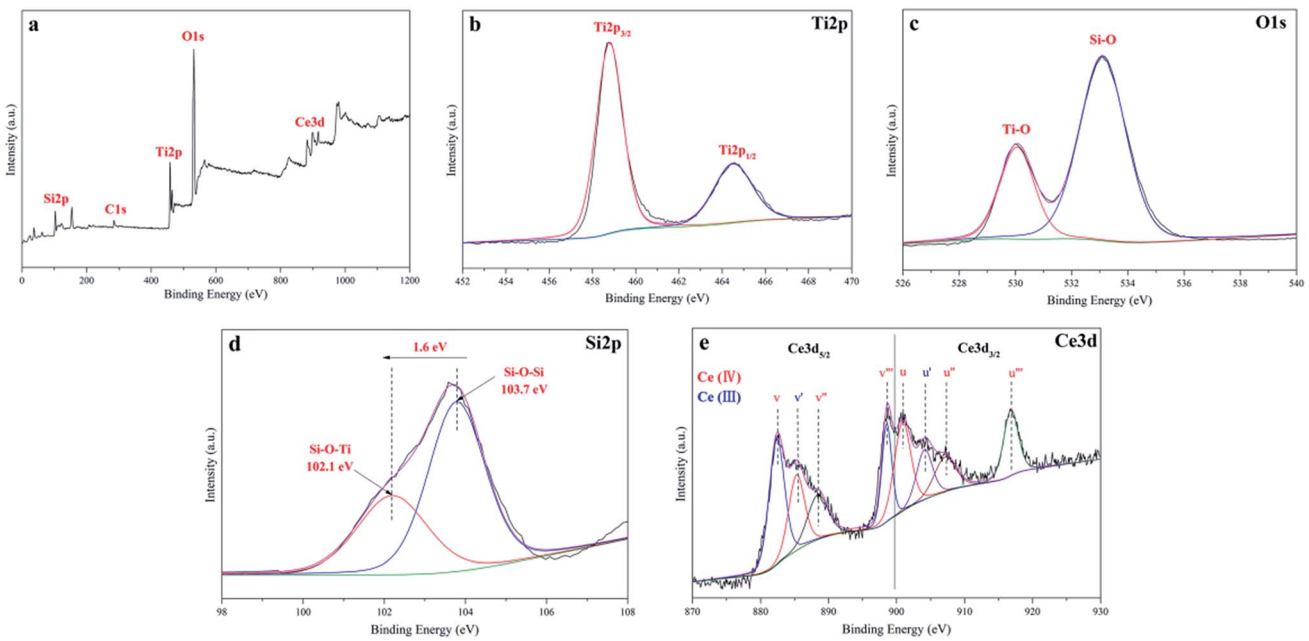

Fig. 3 (a) XPS survey spectra; high resolution XPS spectra of the: (b) Ti 2p, (c) O 1s, (d) Si 2p, and (e) Ce 3d regions of the CSP-5 catalyst.

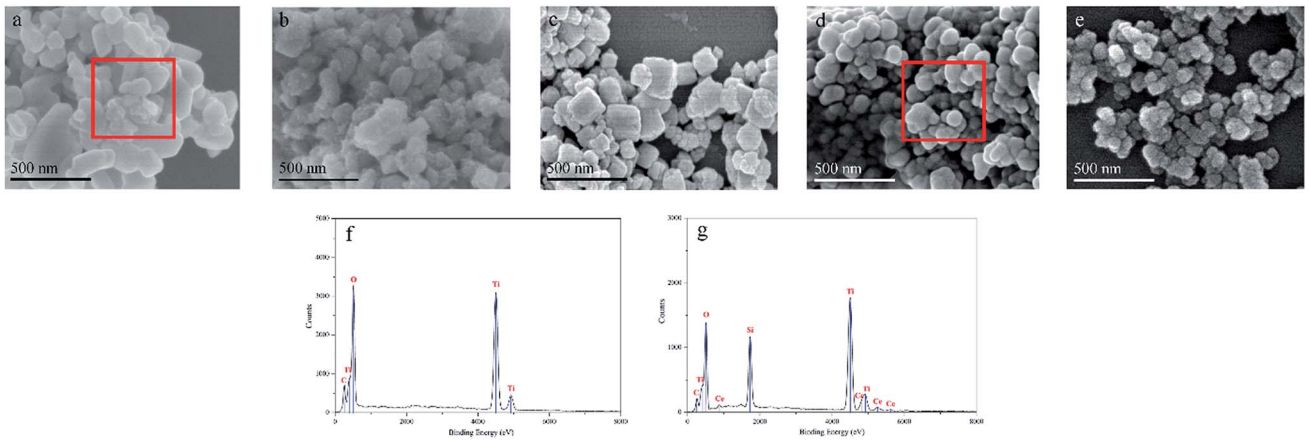

Fig. 4 FE-SEM images of the: (a) P25, (b) CSP-1, (c) CSP-3, (d) CSP-5, and (e) CSP-7 catalysts; EDX of the (f) P25 and (g) CSP-5 catalysts.

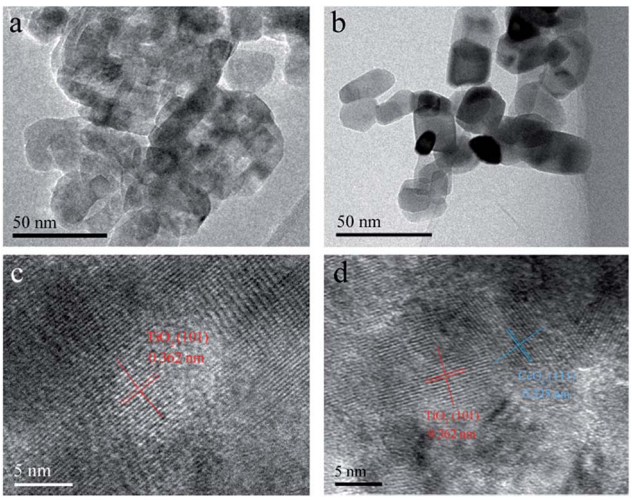

Fig. 5 HRTEM images of (a) P25 and (b) CSP-5; magnified image of the (c) P25 and (d) CSP-5 catalysts.

as 43.9%, 32.5%, 15.6%, and 5.1%, respectively. To further obtain the microscopic structural information, HRTEM analysis of different samples was carried out, and the results are displayed in Fig. 5. The particle size of P25 was about 37.2 nm and serious aggregation can be observed clearly (Fig. 5a). However, after Si and Ce doping it was found that the Ce–SiO_2/TiO_2 sample exhibited the morphology of a loose and homogeneous sphere and had a smaller particle size of 21.8 nm (Fig. 5b), which was in accordance with XRD results that the doped Ce could prevent TiO_2 nanocrystals from aggregating. Clear lattice fringes of the P25 and CSP-5 samples in the magnified HRTEM images can be seen in Fig. 5c and d, in which the interplanar spacing of 0.362 nm and 0.325 nm correspond to the (101) lattice plane of anatase TiO_2 and the (111) lattice plane of CeO_2, respectively.

3.5. Optical properties

3.5.1. UV-vis DRS. UV-vis DRS was performed and the resulting spectra are shown in Fig. 6, which indicate a decrease in the band gap energy of titania in the case of SiO_2/P25 impregnation with Ce. From Fig. 6a, the onset of the absorption spectrum of P25 appears in the UV area, which matches well with the intrinsic band gap of TiO_2. Also, it can be observed that the absorption edge is extended toward higher wavelength for the Ce-doped samples, and it increases with the increasing Ce doping concentration. Among all the samples, the largest red-shift can be found with the Ce-doped SiO_2/P25 sample with 5 mM Ce. The Tauc plot from the Kubelka–Munk function was used to identify the band gap energy, as shown in Fig. 6b. The absorption coefficient α and the indirect band gap (E_g) are related through the following equation:

$$\alpha h\nu = A\left(h\nu - E_g\right)^{\frac{1}{2}} \quad (3)$$

where α represents the absorption coefficient, h is Planck's constant, ν is the radiation frequency, and A is a constant. From the equation, it is possible to obtain a linear plot $(\alpha h\nu)^{1/2}$ *versus* $h\nu$, whose slope is the band gap value. Thus, the E_g of the as-prepared P25, SP, CSP-1, CSP-3, CSP-5, and CSP-7 samples were estimated to 3.02, 2.84, 2.31, 2.23, 2.01, and 2.16 eV respectively. A possible explanation for this phenomenon can be attributed to the presence of Ce^{3+}, as observed from the XPS spectra. CeO_2 has a band gap of about 2.92 eV, and the Ce 4f states are unoccupied. However, the existence of Ce^{3+} leads to an occupation of the 4f band, resulting in a new electronic state among the TiO_2 band gap.[57,58] The distance of charge transfer between the f electrons of the cerium and the conduction (CB) or valence band (VB) of TiO_2 is thus narrowed, thereby allowing the generation of electron–hole pairs using visible light, in which the energy is lower than that required to excite the TiO_2, thus yielding materials with lower band gap values.[59] Hence, these Ce-doped SiO_2/P25 composites show light absorption in the visible region and adequate band gap values to be used as visible-driven photocatalysts. The above information on the physical properties of the prepared catalysts is useful in the following study of photocatalysis.

3.5.2. PL emission. The photoluminescence (PL) emission spectra of all the catalysts are shown in Fig. 7. It is well known that the PL spectra can be used to investigate the efficiency of

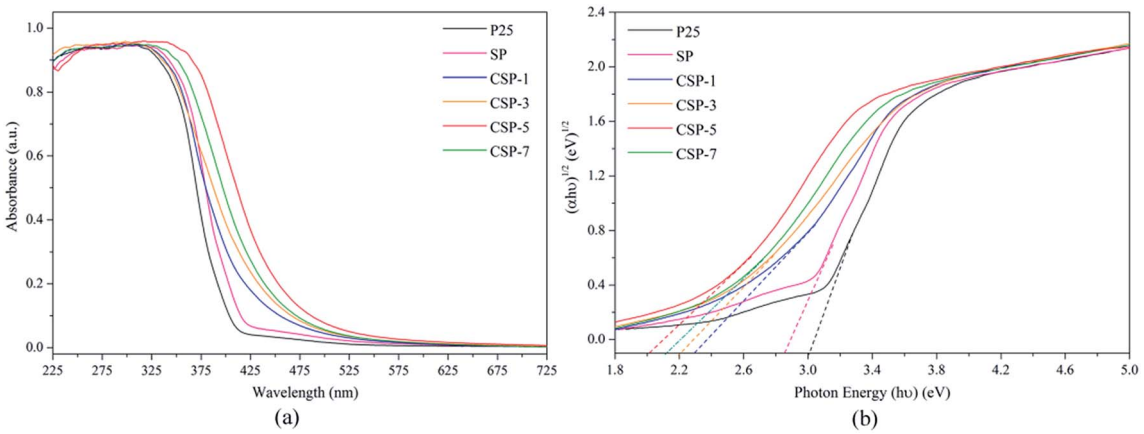

Fig. 6 (a) UV-vis diffuse reflectance spectroscopy and (b) Tauc plot of the as-synthesized catalysts.

charge transfer and electron–hole pairs' separation. PL emission mainly depends on the recombination of electron–hole pairs. A lower emission intensity reveals a decrease in the recombination rate, which is beneficial for improving the photocatalytic activity of catalysts. As can be seen in Fig. 7, the peak positions of the different catalysts were basically the same, showing that the individual loading of silicon and cerium has not induced new photoluminescence. Whereas, the peak intensity of Ce-doped SiO_2/P25 were significantly weaker than that of pure P25, which indicated that the recombination of the photogenerated charge carriers were effectively inhibited. Further inspection of the PL spectra reveal that the CSP-5 sample has the lowest PL intensity compared to the other samples, which suggests that the recombination of photogenerated carriers was highly suppressed due to the cooperative effect of silicon and cerium. This decrease in intensity because of the decreased rate of electron–hole recombination facilitates the production of a large number of ·OH radicals, which enhances the photocatalytic activity for the degradation of pollutants.[60] Nevertheless, it has been reported that excessive metal doping of TiO_2 can adversely cause the acceleration of electron–hole recombination just as much as the CSP-7 material, thus overloading of a metal may not improve the photocatalytic activity.

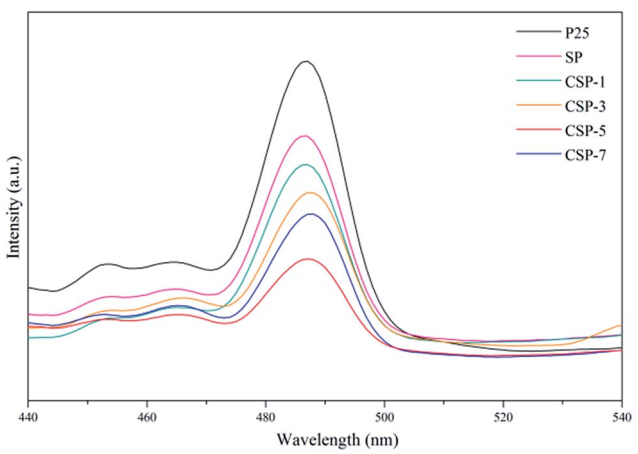

Fig. 7 Photoluminescence emission spectra of all the catalysts.

3.6. Photocatalytic activity

3.6.1. Degradation of organic dyes. The nanocomposites prepared with and without cerium were tested as photocatalysts for the degradation of Methylene Blue (MB) and Reactive Red 4 (RR4) under visible-light irradiation. As indicated, before the photocatalytic reaction, the samples were mixed with the solutions under stirring in the dark for 45 min to reach the adsorption equilibrium. Fig. 8 shows the evolution of MB and RR4 concentration *versus* irradiation time with the P25 and SP/CSP series. Direct photolysis in the absence of any photocatalyst was very small under the experimental conditions and as can be seen, the photocatalytic activity depended on the cerium content of the samples. With the increase in the cerium percentages (for the CSP-1, CSP-3, and CSP-5 samples), there was an improvement in the photocatalytic activity compared with that of the nanocomposite without cerium (SP). However, a further increase in the Ce content resulted in a lower activity (CSP-7). This effect may be due to the structural changes caused by the incorporation of Ce into the TiO_2 lattice. At low cerium concentrations, the structure of the anatase is not modified and the visible absorption becomes obvious, thus the enhanced photocatalytic activity seems to be ascribed to cerium. However, a further increase in the cerium percentage produced a modification of the anatase structure, which reduced the photocatalytic activity. According to Yan *et al.*,[61] the photocatalytic activity was enhanced as a consequence of a lower crystal size at lower cerium amounts, which is in accordance with that observed in our work. Also, the presence of the cerium could effectively capture the photo-induced electrons and holes, while the Ce 4f levels improve the formation of electron–hole pairs, which can eventually enable the Ce^{4+}/Ce^{3+} pairs to interact directly with organic molecules.[62] However, a further increase in the Ce content can also produce recombination of the electron–hole pairs, thus reducing the photocatalytic activity.[63,64] The corresponding results of the photodegradation rate by Ce-doped SiO_2/P25 with different Ce contents and pure P25

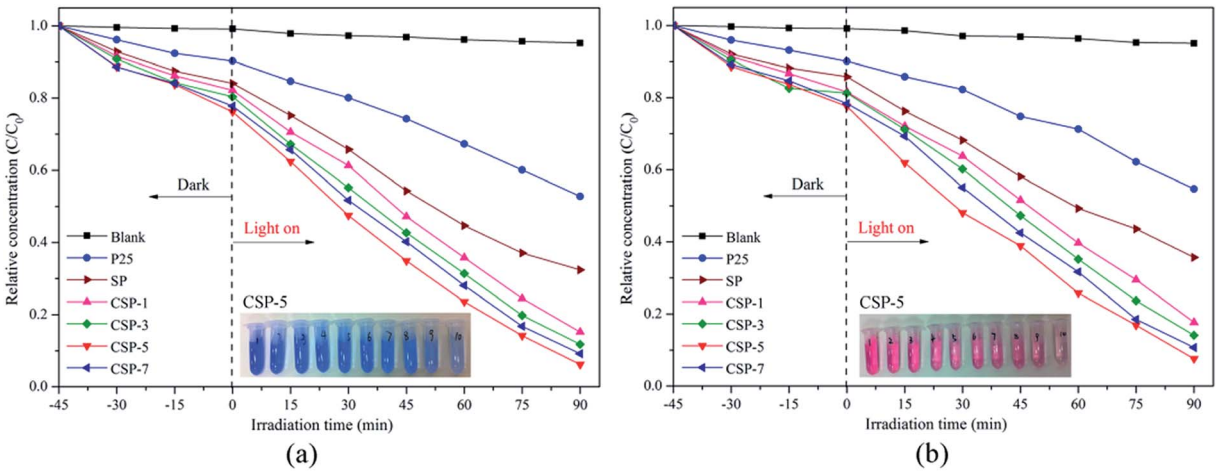

Fig. 8 (a) Photodegradation of (a) MB and (b) RR4 *versus* irradiation time for all the photocatalysts.

under visible light are presented in Fig. 9. The CSP-5 sample shows the best photocatalytic activity of all the samples. The photodegradation rate of this sample could reach over 90% for both MB and RR4 (91.8% for MB and 90.2% for RR4, respectively) after reaction for 90 min, which was more efficient than that of undoped P25 and SP. In order to compare the catalytic activity easily, the results of the photocatalytic activities for different photocatalysts are shown in Table 3. From the table, it can be clearly seen that the photocatalytic activity is in the order of CSP-5 > CSP-7 > CSP-3 > CSP-1 > SP > P25. According to these results, it can be noted that doping with cerium and silicon can be considered as an effective way to improve the photoactivity for preparing TiO_2-based photocatalysts. In addition, the photocatalytic mechanism will be demonstrated concretely in the following section.

The kinetics study of photocatalytic degradation for the different catalysts is discussed using the kinetic model proposed by Langmuir–Hinshelwood[65,66] according to the equation:

$$\ln\left(\frac{C}{C_0}\right) = kt \quad (4)$$

where C_0 is the initial concentration of organic dye once the adsorption equilibrium is reached before lighting the lamp, C is the concentration of the dye after irradiation of the samples in the desired time interval, k is a rate constant, and t is the time. From Fig. 10, a linear relationship between $\ln(C/C_0)$ and the irradiation time could be observed, which suggested that the degradation of MB and RR4 followed first-order reaction kinetics. The kinetics of CSP-5 was almost five times faster than that of the P25 sample, which coincided nicely with higher surface area of the former sample. In accordance with this was the kinetics of the SP sample, which was also faster than the pure TiO_2 sources (Table 4).

Generally, pH is not just an important factor influencing the degradation efficiency of organic compounds in the photocatalytic process but is also a vital variable in the actual treatment of wastewater. Hence, extra experiments were carried out

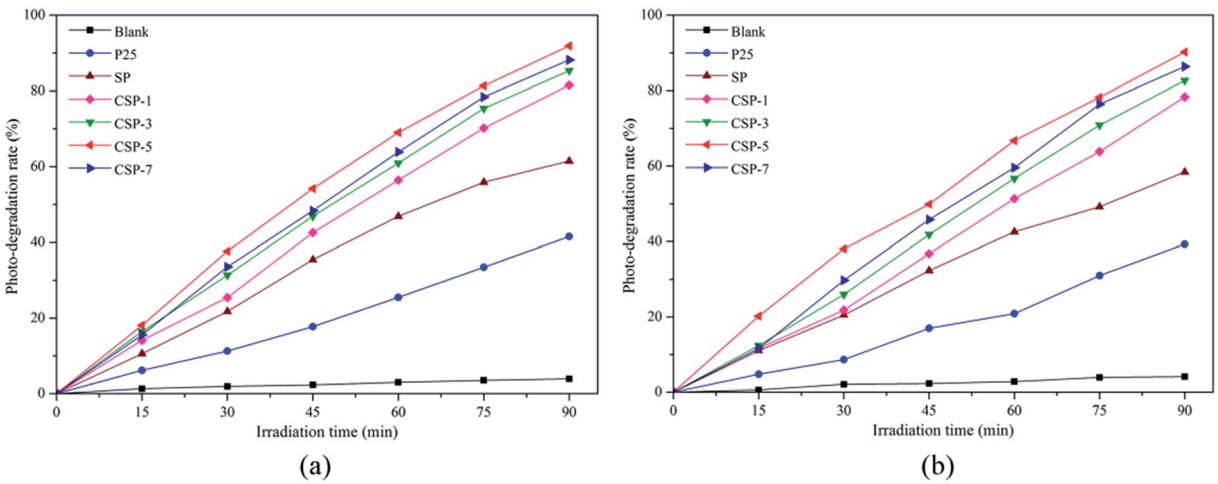

Fig. 9 Degradation efficiency of (a) MB and (b) RR4 *versus* irradiation time for all the photocatalysts.

Table 3 Results of the photocatalytic activities for the different photocatalysts

Degradation of MB			Degradation of RR4		
Catalyst	Relative concentration (C/C_0)	Degradation rate	Catalyst	Relative concentration (C/C_0)	Degradation rate
Blank	0.953	3.93%	Blank	0.951	4.13%
P25	0.528	41.53%	P25	0.547	39.29%
SP	0.324	61.47%	SP	0.357	58.39%
CSP-1	0.152	81.51%	CSP-1	0.177	78.31%
CSP-3	0.118	85.32%	CSP-3	0.141	82.66%
CSP-5	0.062	91.86%	CSP-5	0.087	88.79%
CSP-7	0.092	88.17%	CSP-7	0.107	86.35%

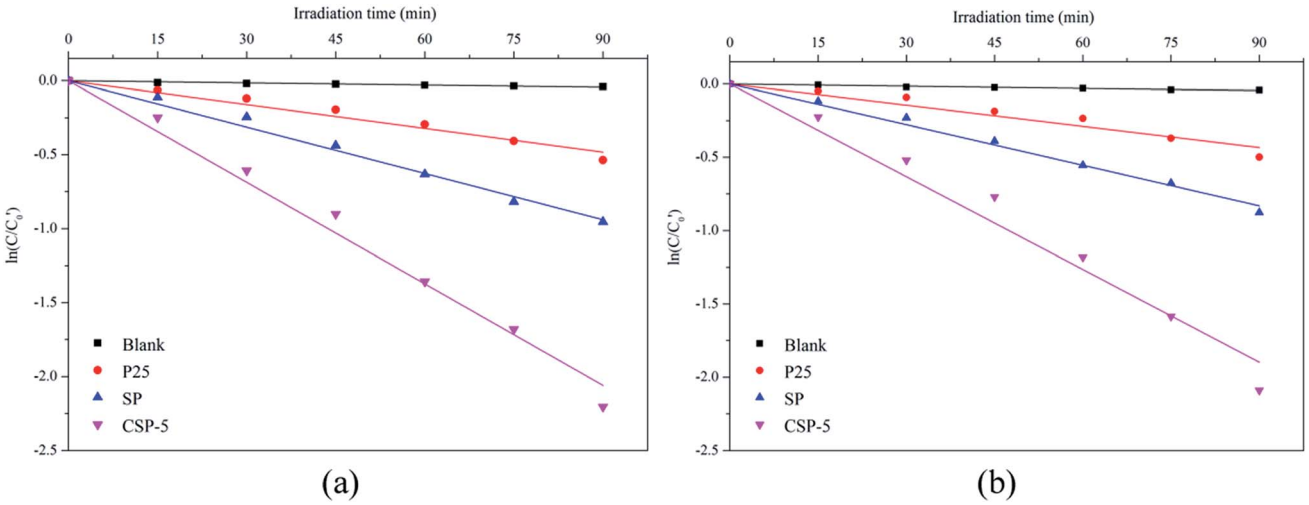

Fig. 10 First-order kinetics for (a) MB and (b) RR4 photocatalytic degradation with various photocatalysts under visible-light irradiation.

to determine the effect of pH on the degradation of MB and RR4 at pH values in the range of 3–11. The strong influence of pH on MB and RR4 photodegradation are shown in Fig. 11. It can be observed from Fig. 11a that the photodegradation rate of MB increased with increasing pH. According to the previous research, the isoelectric point of SiO_2/TiO_2 is 3.00 pH units, resulting in the surface of the catalyst having a negative potential in the range of pH > 3.[38] Since MB is a cationic dye, it is easier to adsorb onto the surface of the catalysts to promote reaction at higher pH. Another possible reason for the result is that there are more hydroxide ions (OH^-) in the alkaline condition that can react with the photogenerated holes to favor the formation of more hydroxyl radicals (·OH), which could significantly enhance the photocatalytic degradation of the dye.[67] On the contrary, it is well known that RR4 is an anionic dye. Based on the theory we mentioned above, the opposite results presented in the anionic RR4 experiment were as expected in Fig. 11b, where it can be seen that the photocatalytic performance of RR4 dropped when going from pH 3 to 11. Therefore, it can be concluded that the influence of pH on photocatalysis is mainly due to the amount of dye adsorbed on the catalysts, and that the degradation takes place at or near the catalyst surface, rather than in the bulk solution.

Table 4 Kinetic features of the catalysts for the degradation of Methylene Blue and Reactive Red 4

Organic pollutants	Catalysts	Rate constant $\times 10^{-3}$ (min^{-1})	R^2
Methylene Blue	Blank	0.49	0.982
	P25	5.36	0.985
	SP	10.45	0.995
	CSP-5	22.88	0.994
Reactive Red 4	Blank	0.51	0.987
	P25	4.81	0.972
	SP	9.24	0.996
	CSP-5	21.08	0.988

3.6.2. Stability of the photocatalysts. One of the most important practical aspects of photocatalysis is the recovery of the used nanocatalyst from suspension and its reuse several times in repeated photocatalytic cycles.[68] The recovery of the nanocatalyst (such as TiO_2) from aqueous suspension becomes easy when such small particles are supported on relatively large size support particles (such as SiO_2).

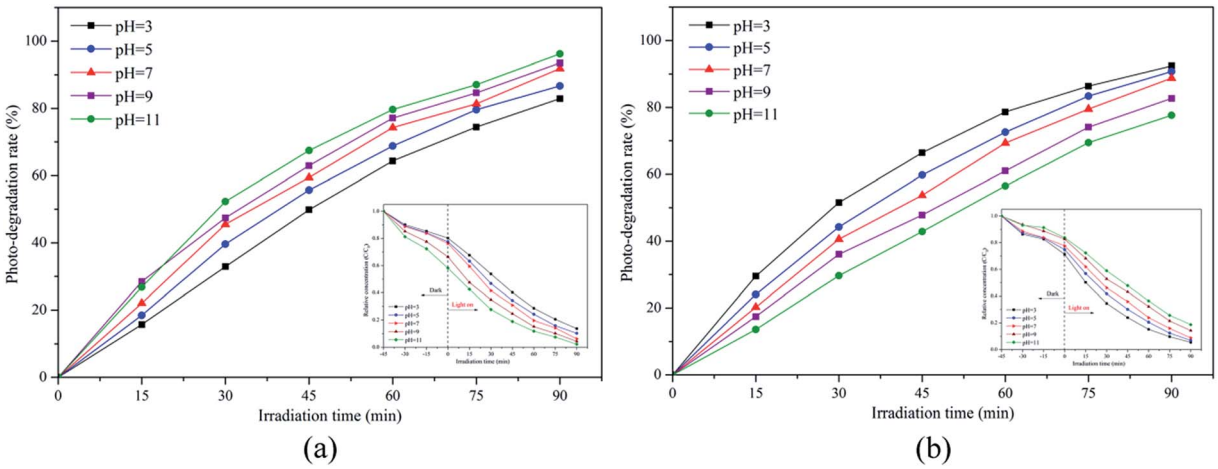

Fig. 11 Effects of the initial pH on the photodegradation of (a) MB and (b) RR4 by the CSP-5 catalyst.

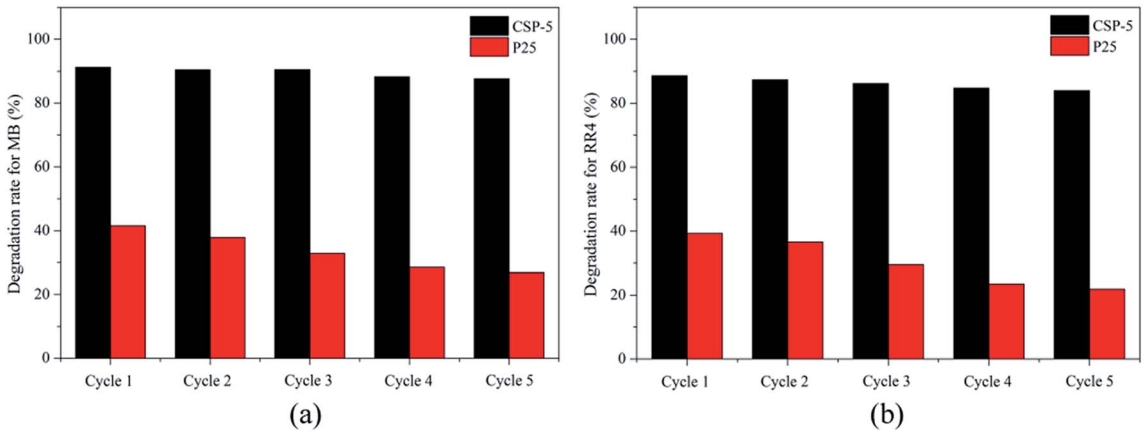

Fig. 12 Photodegradation of (a) MB and (b) RR4 by the recycled P25 and CSP-5 photocatalysts during repeated photocatalytic cycles.

Fig. 12 shows the results of the recycling experiments where the same photocatalyst powder was repeatedly used for up to five times for the photodegradation of MB and RR4. The P25 and CSP-5 catalysts from the first cycle were recovered by centrifugation and reused for the second cycle, and so on. As shown in Fig. 12, the degradation efficiency for both MB and RR4 decreased gradually for both samples after several recycles because active sites on the surface of the samples may be covered by organic substances. Also, some small particles of the catalyst are lost after washing and filtration in each cycle. However, it is clear that the recycled CSPs do not lose their photocatalytic activity upon reuse for up to five times (91.3–87.6% for MB, 88.6–83.9% for RR4) in comparison to pure P25, whereas this difference was higher (41.5–26.9% for MB, 39.3–21.9% for RR4) in the P25 sample. Undoubtedly, we can say that the Ce–SiO_2/P25 sample was a robust and stable catalyst. The CSPs thus offers the advantages of easy recovery by centrifugation and good recyclability due to persistence of the photoactivity of the recycled photocatalyst.

3.6.3. Photoelectrochemical experiments. Since the as-prepared photocatalysts showed the perfect performance in the degradation of the tested dyes, hydrogen evolution experiments were further carried out to investigate the accurate photoelectrochemical properties of the as-prepared samples. Before the actual photoelectrochemical experiments were started, pure ethanol solution was used for the control experiment in the absence of either photocatalyst or irradiation. There was no hydrogen production observed in this experiment. The results therefore excluded other influences of hydrogen generation except from the photocatalytic activities of the as-prepared catalysts. Fig. 13 shows the H_2 evolution of all the catalysts as a function of irradiation time. As the time went on, the generation of hydrogen of all the samples ascended steadily. P25 presented the lowest photocatalytic efficiency in water splitting among all the catalysts, which was only 0.287 mmol g^{-1} after 5 h under visible-light irradiation. Besides, SP performed much better than pure P25, which was 1.294 mmol g^{-1}. As expected, the H_2 evolution rate of the CSPs samples were up to 1.573, 2.019, 2.216, and 2.315 mmol g^{-1}, respectively, higher than SP. This was due to the synergistic effects of silicon and cerium, which could significantly improve the photocatalytic activity of TiO_2. The redox coupling of Ce^{4+}/Ce^{3+} was able to form labile

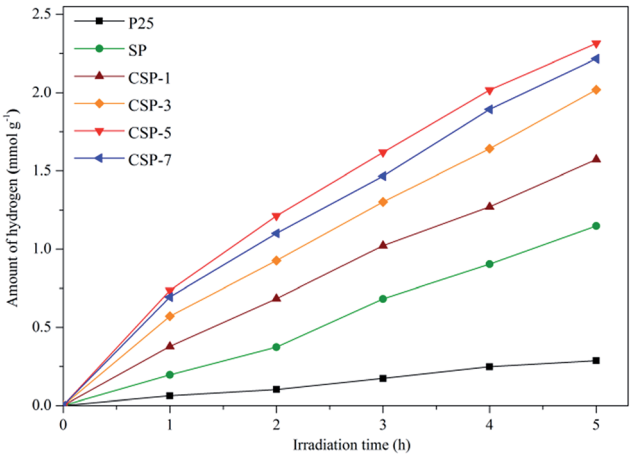

Fig. 13 Visible-light-driven photocatalytic H_2 evolution over all the photocatalysts.

oxygen vacancies with a relatively high mobility of bulk oxygen species, so Ce ions were able to effectively trap conductive band electrons, leading to a high photocatalytic activity. Moreover, Si^{4+} with a higher electronegativity could replace the Ti^{4+} in the TiO_2–SiO_2 composite system, leading to the formation of Si–O–Ti bonds. With the formation of Si–O–Ti bonds, more surface defects may appear. These defects can not only capture the photogenerated electrons or holes but can also increase the reaction activity of hydroxyls, both of which increase the photocatalytic activity of TiO_2.[69,70] It was found that CSP-5 sample had the best photoactivity under the same conditions. However, cerium adversely worked as photogenerated electrons recombination centers when overloaded, as we mentioned in the section covering the photoluminescence emission spectrum. Therefore, it may be suggested that photogenerated electrons recombination should be considered when increasing the visible-light absorption of TiO_2.

3.7. Photocatalytic mechanism

The plausible photocatalytic mechanism is proposed in this section. When the photocatalyst is irradiated by visible light, electron–hole pairs could be generated, which then react with water and dioxygen absorbed on the photocatalyst surface, leading to more oxidized species to form hydroxyl radicals (·OH) and superoxide radical anions (O^{2-}). These oxy radicals can attack organic compounds, including MB and RR4, and decompose them into CO_2 and H_2O. The specific mechanism of photocatalysis mainly includes the following reactions:

$$TiO_2 + h\nu \rightarrow h^+ + e^- \quad (5)$$

$$h^+ + H_2O \rightarrow H^+ + \cdot OH \quad (6)$$

$$O_2 + e^- \rightarrow O_2^- \quad (7)$$

$$O_2^- + e^- + H^+ \rightarrow H_2O_2 \quad (8)$$

$$H_2O_2 \rightarrow \cdot OH \quad (9)$$

$$\cdot OH(O_2^-) + MB/RR4 \rightarrow CO_2 + H_2O \quad (10)$$

However, from the results of the experiments presented in the preceding sections, it turns out that there are many factors that contribute to the enhanced photocatalytic activity of CSPs compared to pure P25, including the following.

3.7.1. Better dispersion of and improved adsorption of organic pollutants. An important difference between the P25 and CSPs samples may be the degree of dispersion of the nanoparticles in suspension. Better dispersion is expected in the case of silica-supported titania,[71,72] while pure P25 very easily forms aggregates in aqueous dispersions.[73] For the supported nanoparticles attached to the silica surface, aggregation is hindered, giving higher accessibility to adsorbates (MB and RR4 in this case). These materials allow an improved probability of photocatalytic reaction, which facilitates the attack by either free or trapped holes.[74–76]

3.7.2. Structural effects. As shown in Fig. 14, the incorporation of Ce dopants can result in a red-shift of the optical absorption edge, indicating that some energy levels are formed on the top of the valence band.[77] From Fig. 14, when the system is irradiated under visible light ($h\nu$ < 3.2 eV), the electrons are more excited from the Ce-doped energy level to arrive at the conduction band of TiO_2. Owing to the enhancement of the visible-light adsorption, the visible-light-induced photocatalytic performance of Ce-doped P25 would also be improved compared to pure P25. As for the Ce^{3+}/Ce^{4+} pairs, they can serve as electron acceptors and superoxide radicals ($\cdot O_2^-$) producers by altering the electron–hole pairs recombination rate.[78] Photogenerated electrons could be trapped by Ce^{4+}, and the Ce^{4+} could reduce to Ce^{3+}. Then, the Ce^{3+} could also be oxidized back to Ce^{4+} by the adsorbed oxygen in this system. Meanwhile, the chemisorbed oxygen could trap the electron of Ce^{3+}, and then produce $\cdot O_2^-$,[79] which can effectively oxidate organic pollutants into CO_2 and H_2O. Ce^{3+}/Ce^{4+} electronic pairs can also capture protons, generating peroxide radicals, or can be further oxidized yielding hydroxide radicals (·OH), whose presence improves the efficiency of the photocatalyst by reacting with the organic pollutants.[80] Therefore, the presence of the Ce^{3+}/Ce^{4+} pairs can not only efficiently separate the electrons and holes but can also result in the generation of $\cdot O_2^-$, thus enhancing

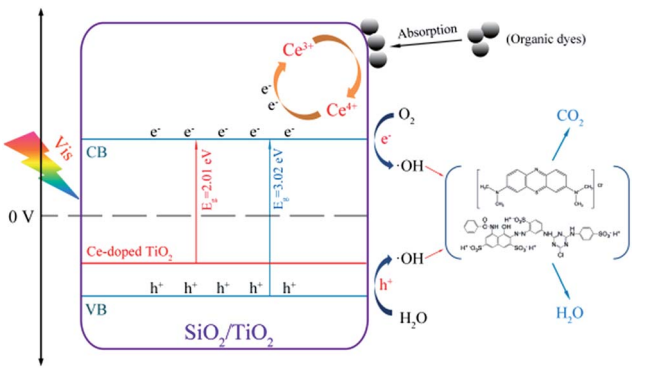

Fig. 14 Photocatalytic mechanism for the photodegradation of organic dyes over Ce–SiO_2/P25 catalyst under visible light.

the occurrence of ·OH for the degradation of the organic molecules. However, excess Ce species might cover the active sites or act as a recombination center of TiO_2, which can result in the decrease the photocatalytic activity and in the separation efficiency of the charge carriers, as discussed in Section 3.5.2.

In summary, the enhanced photoactivity of CSPs compared to pristine P25 may thus be attributed to a combined effect involving a better dispersion of the supported TiO_2, a good adsorption of organic molecules, and the formation of new energy levels on the CSPs.

4. Conclusions

Low-cost Ce–SiO_2/P25 nanoparticles (denoted as CSPs in this article) were prepared using an environmentally friendly approach involving precipitation of a colloidal solution of Degussa P25 nanoparticles with TEOS and peptization with $Ce(NO_3)_3$, at low temperature and at ambient pressure. The formed CSPs had a high BET surface area, small crystallite size, and large pore volume, which was beneficial for enhancing the adsorption of organic pollutants on the catalyst surface before their degradation. The CSPs were evaluated as a kind of Ce–SiO_2/TiO_2 composite in the form of powders for the total decomposition of Methylene Blue (MB) and Reactive Red 4 (RR4) as model organic pollutants. In particular, the CSP-5 nanoparticle was the most effective photocatalyst for the degradation of organic dyes under visible-light irradiation, and showed 91.8% decomposition of MB and 90.2% decomposition of RR4 in the liquid phase, at room temperature. The results indicated that the increase in photocatalytic activity of the CSP-5 sample resulted from the combination of a quantum size effect with the reduced size of the nanocrystals, new energy levels, and enhanced adsorption of the pollutants due to the SiO_2 support. Another operative condition was studied for further practical application. The optimal solution pH for RR4 and MB was found to be equal to 3 and 11, respectively. Since real wastewater is a mixture of many pollutants, it is important to design a photocatalyst that addresses as many of them in the highest decomposition efficiency possible. The two contaminants used in this study (MB and RR4) are considered as surrogates for two major classes (cationic and anionic dyes) of water contaminants, which represent a good choice for testing the efficiency of newly synthesized photocatalysts. We expect our work could give a new way of thinking about the exploration of TiO_2 photocatalysts.

Acknowledgements

The author would like to thank Beijing Jiaotong University and the State Key Laboratory of Solid Wastes Resource Utilization and Energy Saving Building Materials in Beijing Building Materials Academy of Science Research. This work was financially supported by Beijing Jiaotong University Foundation (2012RC002), the National Science Foundation of China (Grant no. 11475017), the State Key Laboratory of Solid Wastes Resource Utilization and Energy Saving Building Materials (SWR-2013-009) and the Fundamental Research Funds for the Central Universities (2014JBZ010). Yan Jiang would also like to express his gratitude to all colleagues who provided assistance.

References

1 K. Kümmerer, in *Pharmaceuticals in the Environment: Sources, Fate, Effects and Risk*, ed. K. Kümmerer, Springer, New York, 2004, pp. 3–11.
2 D. Maycock and C. Watts, in *Encyclopedia of Environmental Health*, ed. J. Nriagu, Elsevier, Burlington, 2011, pp. 472–484.
3 A. Fujishima and K. Honda, Electrochemical photocatalysis of water at semiconductor electrode, *Nature*, 1972, **238**, 37–38.
4 X. Chen and A. Selloni, Introduction: titanium dioxide (TiO_2) nanomaterials, *Chem. Rev.*, 2014, **114**, 9281–9282.
5 A. Linsebigler, G. Lu and J. Yates, Photocatalysis on TiO_2 surfaces: principles, mechanisms, and selected results, *Chem. Rev.*, 1995, **95**, 735–758.
6 A. Fujishima, X. Zhang and D. Tryk, TiO_2 photocatalysis and related surface phenomena, *Surf. Sci. Rep.*, 2008, **63**, 515–582.
7 E. Pakdel and W. Daoud, Self-cleaning cotton functionalized with TiO_2/SiO_2: focus on the role of silica, *J. Colloid Interface Sci.*, 2013, **401**, 1–7.
8 S. Son, S. Hwang, C. Kim, J. Yun and J. Jang, Designed synthesis of SiO_2/TiO_2 core/shell structure as light scattering material for highly efficient dye-sensitized solar cells, *ACS Appl. Mater. Interfaces*, 2013, **5**, 4815–4820.
9 Y. Li, P. Leung, L. Yao, Q. Song and E. Newton, Antimicrobial effect of surgical masks coated with nanoparticles, *J. Hosp. Infect.*, 2006, **62**, 58–63.
10 D. Sheel and P. Evans, Photoactive and antibacterial TiO_2 thin films on stainless steel, *Surf. Coat. Technol.*, 2007, **201**, 9319–9324.
11 K. Saravanan, K. Ananthanarayanan and P. Balaya, Mesoporous TiO_2 with high packing density for superior lithium storage, *Energy Environ. Sci.*, 2010, **3**, 939–948.
12 J. Schneider, M. Matsuoka, M. Takeuchi, J. Zhang, Y. Horiuchi, M. Anpo and D. W. Bahnemann, Understanding TiO_2 photocatalysis: mechanisms and materials, *Chem. Rev.*, 2014, **114**, 9919–9986.
13 M. Dahl, Y. Liu and Y. Yin, Composite titanium dioxide nanomaterials, *Chem. Rev.*, 2014, **114**, 9853–9889.
14 Y. Wang, W. Duan, B. Liu, X. Chen, F. Yang and J. Guo, The effect of doping copper and mesoporous structure on photocatalytic properties of TiO_2, *J. Nanomater.*, 2014, **178152**, 7.
15 N. Mandzy, E. Grulke and T. Druffel, Breakage of TiO_2 agglomerates in electrostatically stabilized aqueous dispersions, *Powder Technol.*, 2005, **160**, 121–126.
16 D. Hanaor, M. Assadi, S. Li, A. Yu and C. Sorrell, *Ab initio* study of phase stability in doped TiO_2, *Comput. Mech.*, 2012, **50**, 185–194.
17 K. Raj and B. Viswanathan, Effect of surface area, pore volume and particle size of P25 titania on the phase transformation of anatase to rutile, *Indian J. Chem.*, 2009, **48**, 1378–1382.

18 J. Herrmann, Heterogeneous photocatalysis: fundamentals and applications to the removal of various types of aqueous pollutants, *Catal. Today*, 1999, **53**, 115–129.
19 A. Hanprasopwattana, T. Rieker, A. Sault and A. Datye, Morphology of titania coatings on silica gel, *Catal. Lett.*, 1997, **45**, 165–175.
20 R. Iler, *The chemistry of Silica*, Wiley-Interscience, New York, 1978.
21 A. Fink, W. Stöber and E. Bohn, Controlled growth of monodisperse silica spheres in the micron size range, *J. Colloid Interface Sci.*, 1968, **26**, 62–69.
22 S. Ullah, E. Ferreira-Neto, A. Pasa, C. Alcântara, J. Acuna, S. Bilmes, M. Ricci, R. Landers, T. Fermino and U. Rodrigues-Filho, Enhanced photocatalytic properties of core@shell SiO_2@TiO_2 nanoparticles, *Appl. Catal., B*, 2015, **179**, 333–343.
23 G. Tian, H. Fu, L. Jing, B. Xin and K. Pan, Preparation and characterization of stable biphase TiO_2 photocatalyst with high crystallinity, large surface area, and enhanced photoactivity, *J. Phys. Chem. C*, 2008, **112**, 3083–3089.
24 H. Zhu, Z. Ma, S. Overbury and S. Dai, Rational design of gold catalysts with enhanced thermal stability: post modification of Au/TiO_2 by amorphous SiO_2 decoration, *Catal. Lett.*, 2007, **116**, 128–135.
25 P. Periyat, K. Baiju, P. Mukundan, P. Pillai and K. Warrier, High temperature stable mesoporous anatase TiO_2 photocatalyst achieved by silica addition, *Appl. Catal., A*, 2008, **349**, 13–19.
26 S. Rasalingam, R. Peng and R. Koodali, Removal of hazardous pollutants from wastewaters: applications of TiO_2–SiO_2 mixed oxide materials, *J. Nanomater.*, 2014, **617405**, 42.
27 C. Anderson and A. Bard, An improved photocatalyst of TiO_2/SiO_2 prepared by a sol–gel synthesis, *J. Phys. Chem.*, 1995, **99**, 9882–9885.
28 P. Cheng, M. Zheng, Y. Jin, Q. Huang and M. Gu, Preparation and characterization of silica-doped titania photocatalyst through sol–gel method, *Mater. Lett.*, 2003, **57**, 2989–2994.
29 G. Calleja, D. Serrano, R. Sanz and P. Pizarro, Mesostructured SiO_2-doped TiO_2 with enhanced thermal stability prepared by a soft-templating sol–gel route, *Microporous Mesoporous Mater.*, 2008, **111**, 429–440.
30 J. Aguado, R. Grieken, M. López-Muñoz and J. Marugán, Comprehensive study of the synthesis, characterization and activity of TiO_2 and mixed TiO_2/SiO_2, *Appl. Catal., A*, 2006, **312**, 202–212.
31 Y. Cong, B. Tian and J. Zhang, Improving the thermal stability and photocatalytic activity of nanosized titanium dioxide *via* La^{3+} and N co-doping, *Appl. Catal., B*, 2011, **101**, 376–381.
32 S. Sajjad, S. Leghari, F. Chen and J. Zhang, Bismuth-doped ordered mesoporous TiO_2: visible-light catalyst for simultaneous degradation of phenol and chromium, *Chem.–Eur. J.*, 2010, **16**, 13795–13804.
33 W. Wang, J. Zhang, F. Chen, M. Anpo and D. He, Catalysis of redox reactions by Ag@TiO_2 and Fe^{3+}-doped Ag@TiO_2 core–shell type nanoparticles, *Res. Chem. Intermed.*, 2010, **36**, 163–172.
34 X. Yuan, J. Zhang, M. Anpo and D. He, Synthesis of Fe^{3+} doped ordered mesoporous TiO_2 with enhanced visible light photocatalytic activity and highly crystallized anatase wall, *Res. Chem. Intermed.*, 2010, **36**, 83–88.
35 M. Nasir, F. Zhang and B. Tian, Detailed study of Ce and C codoping on the visible light response of titanium dioxide, *Res. Chem. Intermed.*, 2015, **41**, 1607–1624.
36 M. Nasir, S. Bagwasi, Y. Jiao, F. Chen, B. Tian and J. Zhang, Characterization and activity of the Ce and N co-doped TiO_2 prepared through hydrothermal method, *Chem. Eng. J.*, 2014, **236**, 388–397.
37 V. Stengl, S. Bakardjieva and N. Murafa, Preparation and photocatalytic activity of rare earth doped TiO_2 nanoparticles, *Mater. Chem. Phys.*, 2009, **114**, 217–226.
38 Y. Liu, H. Yu, Z. Lv, S. Zhan, J. Yang, X. Peng, Y. Ren and X. Wu, Simulated-sunlight-activated photocatalysis of Methylene Blue using cerium-doped SiO_2/TiO_2 nanostructured fibers, *J. Environ. Sci.*, 2012, **24**, 1867–1875.
39 S. Pavasupree, Y. Suzuki, S. Pivsa-Art and S. Yoshikawa, Preparation and characterization of mesoporous TiO_2–CeO_2 nanopowders respond to visible wavelength, *J. Solid State Chem.*, 2005, **178**, 128–134.
40 B. Reddy, A. Khan, Y. Yamada, T. Kobayashi, S. Loridant and J. C. Volta, Surface characterization of CeO_2/SiO_2 and V_2O_5/CeO_2/SiO_2 catalysts by Raman, XPS, and other techniques, *J. Phys. Chem. B*, 2002, **106**, 10964–10972.
41 F. Li, X. Li, M. Hou, K. Cheah and W. Choy, Enhanced photocatalytic activity of Ce^{3+}–TiO_2 for 2-mercaptobenzothiazole degradation in aqueous suspension for odour control, *Appl. Catal., A*, 2005, **285**, 181–189.
42 M. Fernández-García, A. Martínez-Arias, J. Hanson and J. Rodríguez, Nanostructured oxides in chemistry: characterization and properties, *Chem. Rev.*, 2004, **104**, 4063–4104.
43 S. Ito, P. Chen, P. Comte, M. Nazeeruddin, P. Liska and P. Pechy, Fabrication of screen printing pastes from TiO_2 powders for dye-sensitised solar cells, *Prog. Photovoltaics*, 2007, **15**, 603–612.
44 J. Zhang, Z. Huang, Y. Xu and F. Kang, Carbon-coated TiO_2 composites for the photocatalytic degradation of low concentration benzene, *New Carbon Materials*, 2011, **26**, 63–70.
45 A. Suligoj, U. Stangara, A. Ristic, M. Mazaj, D. Verhovsek and N. Tusar, TiO_2–SiO_2 films from organic-free colloidal TiO_2 anatase nanoparticles as photocatalyst for removal of volatile organic compounds from indoor air, *Appl. Catal., A*, 2016, **184**, 119–131.
46 A. Xu, Y. Gao and H. Liu, The preparation, characterization, and their photocatalytic activities of rare-earth-doped TiO_2 nanoparticles, *J. Catal.*, 2002, **207**, 151–157.
47 J. Xu, Y. Ao and D. Fu, A novel Ce,C-codoped TiO_2 nanoparticles and its photocatalytic activity under visible light, *Appl. Surf. Sci.*, 2009, **256**, 884–888.

48 K. Sing, Reporting physisorption data for gas/solid systems with special reference to the determination of surface area and porosity, *Pure Appl. Chem.*, 1982, **54**, 2208–2218.
49 M. Kruk and M. Jaroniec, Gas adsorption characterization of ordered organic–inorganic nanocomposite materials, *Chem. Mater.*, 2001, **13**, 3169–3183.
50 J. Yu, J. Yu, M. Leung, W. Ho, B. Cheng, X. Zhao and J. Zhao, Effects of acidic and basic hydrolysis catalysts on the photocatalytic activity and microstructures of bimodal mesoporous titania, *J. Catal.*, 2003, **217**, 69–78.
51 Y. Cao, W. Yang, W. Zhang, G. Liu and P. Yue, Improved photocatalytic activity of Sn^{4+} doped TiO_2 nanoparticulate films prepared by plasma-enhanced chemical vapor deposition, *New J. Chem.*, 2004, **28**, 218–222.
52 B. Erdem, R. Hunsicker, G. Simmons, E. Sudol, V. Dimonie and M. El-Aasser, XPS and FTIR surface characterization of TiO_2 particles used in polymer encapsulation, *Langmuir*, 2001, **17**, 2664–2669.
53 M. Nasir, Z. Xi, M. Xing, J. Zhang, F. Chen, B. Tian and S. Bagwasi, Study of synergistic effect of Ce- and S-codoping on the enhancement of visible-light photocatalytic activity of TiO_2, *J. Phys. Chem. C*, 2013, **117**, 9520–9528.
54 T. Gross, M. Ramm, H. Sonntag, W. Unger, H. Weijers and E. Adem, An XPS analysis of different SiO_2 modifications employing a C1s as well as an $Au4f_{7/2}$ static charge reference, *Surf. Interface Anal.*, 1992, **18**, 59–64.
55 E. Paparazzo, G. Ingo and N. Zacchetti, X-ray induced reduction effects at CeO_2 surfaces: an X-ray photoelectron spectroscopy study, *J. Vac. Sci. Technol., A*, 1991, **9**, 1416–1420.
56 S. Yang, W. Zhu, J. Wang and Z. Chen, The surface properties and the activities in catalytic wet air oxidation over CeO_2–TiO_2 catalysts, *J. Hazard. Mater.*, 2008, **153**, 1248–1253.
57 N. Skorodumova, R. Ahuja, S. Simak, I. Abrikosov, B. Johansson and B. Lundqvist, Electronic, bonding, and optical properties of CeO_2 and Ce_2O_3 from first principles, *Phys. Rev. B: Condens. Matter Mater. Phys.*, 2001, **64**, 115108.
58 D. Andersson, S. Simak, B. Johansson, I. Abrikosov and N. Skorodumova, Modeling of CeO_2, Ce_2O_3, and CeO_{2-x} in the LDA+U formalism, *Phys. Rev. B: Condens. Matter Mater. Phys.*, 2007, **75**, 035109.
59 C. Belver, R. Bellod, S. Stewart, F. Requejo and M. Fernandez-Garcia, Nitrogen-containing TiO_2 photocatalysts: part 2. Photocatalytic behavior under sunlight excitation, *Appl. Catal., B*, 2006, **65**, 309–314.
60 Z. Jin, W. Duan, B. Liu, X. Chen, F. Yang and J. Guo, Fabrication of efficient visible light activated Cu–P25–graphene ternary composite for photocatalytic degradation of methyl blue, *Appl. Surf. Sci.*, 2015, **356**, 707–718.
61 N. Yan, Z. Zhu, J. Zhang, Z. Zhao and Q. Liu, Preparation and properties of Ce-doped TiO_2 photocatalyst, *Mater. Res. Bull.*, 2012, **47**, 1869–1873.
62 Y. Xie and C. Yuan, Visible-light responsive cerium ion modified titania sol and nanocrystallites for X-3B dye photodegradation, *Appl. Catal., B*, 2003, **46**, 251–259.
63 K. Nagaveni, M. Hegde and G. Madras, Structure and photocatalytic activity of $Ti_{1-x}M_xO_2 \pm$ delta (M = W, V, Ce, Zr, Fe, and Cu) synthesized by solution combustion method, *J. Phys. Chem. B*, 2004, **108**, 20204–20212.
64 S. Ikeda, N. Sugiyama, B. Pal, G. Marc, L. Palmisano, H. Noguchi, K. Uosakid and B. Ohtani, Photocatalytic activity of transition-metal-loaded titanium(IV) oxide powders suspended in aqueous solutions: correlation with electron hole recombination kinetics, *Phys. Chem. Chem. Phys.*, 2001, **3**, 267–273.
65 Y. Chiang and C. Lin, Photocatalytic decolorization of methylene blue in aqueous solutions using coupled ZnO/SnO_2 photocatalysts, *Powder Technol.*, 2013, **246**, 137–143.
66 S. Kansal, G. Kaur and S. Singh, Studies on the photocatalytic degradation of 2,3-dichlorophenol using different oxidants in aqueous solutions, *React. Kinet. Catal. Lett.*, 2009, **98**, 177–186.
67 C. Wang, C. Lee, M. Lyu and L. Juang, Photocatalytic degradation of C.I. basic violet 10 using TiO_2 catalysts supported by Y zeolite: an investigation of the effects of operational parameters, *Dyes Pigm.*, 2008, **76**, 817–824.
68 X. Li, X. Wu, G. He, J. Sun, W. Xiao and Y. Tan, Microspheroidization treatment of macroporous TiO_2 to enhance its recycling and prevent membrane fouling of photocatalysis-membrane system, *Chem. Eng. J.*, 2014, **251**, 58–68.
69 X. Gao and I. Wachs, Titania–silica as catalysts: molecular structural characteristics and physico-chemical properties, *Catal. Today*, 1999, **51**, 233–254.
70 Y. Yao, N. Zhao, J. Feng, M. Yao and F. Li, Photocatalytic activities of Ce or Co doped nanocrystalline TiO_2–SiO_2 composite films, *Ceram. Int.*, 2013, **39**, 4735–4738.
71 A. Li, Y. Jin, D. Muggli, D. Pierce, H. Aranwela, G. Marasinghe, T. Knutson, G. Brockman and X. Zhao, Nanoscale effects of silica particle supports on the formation and properties of TiO_2 nanocatalysts, *Nanoscale*, 2013, **5**, 5854–5862.
72 M. Hirano, K. Ota and H. Iwata, Formation of anatase (TiO_2)/silica (SiO_2) composite nanoparticles with high phase stability of 1300 °C from acidic solution by hydrolysis under hydrothermal condition, *Chem. Mater.*, 2004, **16**, 3725–3732.
73 R. Pagel and J. Dohtmann, Thermochemical study of photoinduced processes at TiO_2 nanoparticles in aqueous suspension containing Br^- or Cl^-. Photodeaggregation and subsequent processes, *J. Phys. Chem. C*, 2007, **111**, 4458–4464.
74 C. Minero, F. Catozzo and E. Pelizzetti, Role of adsorption in photocatalyzed reactions of organic molecules in aqueous titania suspensions, *Langmuir*, 1992, **8**, 481–486.
75 D. Friesen, L. Morello, J. Headley and C. Langford, Factors influencing relative efficiency in photo-oxidations of organic molecules by $Cs_3PW_{12}O_{40}$ and TiO_2 colloidal photocatalysts, *J. Photochem. Photobiol., A*, 2000, **133**, 213–220.

76 Y. Xu and C. Langford, UV- or visible-light-induced degradation of X3B on TiO_2 nanoparticles: the influence of adsorption, *Langmuir*, 2001, **17**, 897–902.
77 S. Song, L. Xu, Z. He, J. Chen, X. Xiao and B. Yan, Mechanism of the photocatalytic degradation of CI Reactive Black 5 at pH 12.0 using $SrTiO_3/CeO_2$ as the catalyst, *Environ. Sci. Technol.*, 2007, **41**, 5846–5853.
78 Q. Chen, D. Jiang, W. Shi, D. Wu and Y. Xu, Visible-light-activated Ce–Si co-doped TiO_2 photocatalyst, *Appl. Surf. Sci.*, 2009, **255**, 7918–7924.
79 E. Kozlova, T. Korobkina, A. Vorontsov and V. Parmon, Enhancement of the O_2- or H_2-photoproduction rate in a Ce^{3+}/Ce^{4+}–TiO_2 system by the TiO_2 surface and structure modification, *Appl. Catal., A*, 2009, **367**, 130–137.
80 N. Yan, Z. Zhu, J. Zhang, Z. Zhao and Q. Liu, Preparation and properties of Ce-doped TiO_2 photocatalyst, *Mater. Res. Bull.*, 2012, **47**, 1869–1873.

